Preprint typeset in JHEP style - HYPER VERSION

DEMNUni: ISW, Rees-Sciama, and weak-lensing in the presence of massive neutrinos

Carmelita Carbone

INAF–Osservatorio Astronomico di Brera, Via Bianchi 46, 23807, Merate (MI), Italy
INFN–Sezione di Bologna, viale Berti Pichat 6/2, I-40127, Bologna (BO), Italy
E-mail: carmelita.carbone@brera.inaf.it

Margarita Petkova

Excellence Cluster Universe, Boltzmannstr. 2, D-85748 Garching, Germany
Universitäts-Sternwarte, Fakultät für Physik, Ludwig-Maximilians Universität München, Scheinerstr. 1, D-81679 München, Germany
E-mail: mpetkova@usm.lmu.de

Klaus Dolag

Universitäts-Sternwarte, Fakultät für Physik, Ludwig-Maximilians Universität München, Scheinerstr. 1, D-81679 München, Germany
Max-Planck-Institut für Astrophysik, Karl-Schwarzschild Strasse 1, Garching bei München, Germany
E-mail: kdolag@mpa-garching.mpg.de

Abstract: We present, for the first time in the literature, a full reconstruction of the total (linear and non-linear) ISW/Rees-Sciama effect in the presence of massive neutrinos, together with its cross-correlations with CMB-lensing and weak-lensing signals. The present analyses make use of all-sky maps extracted via ray-tracing across the gravitational potential distribution provided by the "Dark Energy and Massive Neutrino Universe" (DEMNUni) project, a set of large-volume, high-resolution cosmological N-body simulations, where neutrinos are treated as separate collisionless particles. We correctly recover, at $1-2\%$ accuracy, the linear predictions from CAMB. Concerning the CMB-lensing and weak-lensing signals, we also recover, with similar accuracy, the signal predicted by Boltzmann codes, once non-linear neutrino corrections to Halofit are accounted for. Interestingly, in the ISW/Rees-Sciama signal, and its cross correlation with lensing, we find an excess of power with respect to the massless case, due to free streaming neutrinos, roughly at the transition scale between the linear and non-linear regimes. The excess is $\sim 5-10\%$ at $l \sim 100$ for the ISW/Rees-Sciama auto power spectrum, depending on the total neutrino mass M_ν, and becomes a factor of ~ 4 for $M_\nu = 0.3$ eV, at $l \sim 600$, for the ISW/Rees-Sciama cross power with CMB-lensing. This effect should be taken into account for the correct estimation of the CMB temperature bispectrum in the presence of massive neutrinos.

Keywords: cosmology: neutrinos, ISW, Rees-Sciama, weak-lensing, CMB-lensing.

Contents

1. Introduction

The Standard Model of particle physics predicts the existence of three active massless neutrino species: the electron ($\nu_{\rm e}$), muon (ν_μ) and tau (ν_τ) neutrinos. However, the discovery of lepton flavour oscillations has suggested that neutrinos are massive particles, fixing the lower limit of the sum of neutrino masses to $\Sigma\, m_\nu \equiv m_{\nu_e} + m_{\nu_\mu} + m_{\nu_\tau} \gtrsim 0.06$ eV[1] [1, 2, 3, 4]. This implies that, after becoming non-relativistic, neutrino free-stream with large thermal velocities that suppress the growth of neutrino densities perturbations on scales smaller than the so-called "free-streaming length", $\lambda_{\rm fs}(z, m_\nu) \simeq 8.1\, H_0\, (1+z)/H(z)\, (1\,{\rm eV/m_\nu})\,{\rm Mpc/h}$, where m_ν is the mass of the single neutrino species, $H(z)$ is the so-called Hubble parameter, and H_0 the Hubble constant, $H(z=0)$. As a consequence, due to gravitational backreaction effects, also the evolution of cold dark matter (CDM) and baryon [5] densities is altered, and the total matter power spectrum is largely suppressed at scales $\lambda << \lambda_{\rm fs}$.

Moreover, given the present mass constraints, neutrinos become non-relativistic after the epoch of recombination, and, accordingly, modify the radiation density contribution. The transition from the relativistic to the non-relativistic regimes postpones the matter radiation equality for a given value of $\Omega_{\rm m}\, h^2$ (where $\Omega_{\rm m}$ is the ratio, at $z=0$, between the matter density of the Universe and the critical density, $\rho_{\rm c}$, and h the Hubble constant H_0 in units of 100 km s^{-1}Mpc^{-1}), and modifies the background evolution, slightly affecting the properties of the primary cosmic microwave background (CMB) anisotropies.

[1] More specifically, $\Sigma\, m_\nu$ must be greater than approximately 0.06 eV in the normal hierarchy scenario and 0.1 eV in the degenerate hierarchy.

In addition, along their travel from the last scattering surface to the observer, CMB photons undergo also secondary anisotropies, in particular they are red/blue-shifted as they cross growing/decaying gravitational potential wells. This effect is called the late Integrated Sachs-Wolfe effect (ISW), as it was first described by Sachs and Wolfe in 1967 [6]. During the matter dominated era, the two effects of background expansion and gravitational attraction compensate each other so that the total linear gravitational potential, Φ, produced by the Large Scale Structure (LSS) distribution in the Universe, is constant in time, and the ISW effect, which depends on the time derivative $\dot{\Phi}$, vanishes. In contrast, during *e.g.* the Dark Energy (DE) dominated era, the background expansion rate of the Universe increases and these two effects do not compensate anymore, causing the decaying of the gravitational potential perturbations. In this case, $\dot{\Phi}$ is no longer vanishing: a CMB photon passing through an overdense region gains more energy falling into the potential well with respect to the energy lost while climbing out of it; a CMB photon passing through an underdense region loses more energy climbing the potential hill than the energy gained during its descent. Therefore, overdense regions correspond to hotter spots in the CMB sky map, and underdense regions to colder ones.

In the linear regime, the total effect is represented by an increase of the photon temperature power spectrum on very large scales, which has actually been detected via full-sky CMB probes, *e.g.* Planck [7, 8], or via the cross-correlation of the CMB temperature with LSS data [9, 10, 11].

However, besides dark energy, also the cosmological background of massive neutrinos produces a non-vanishing ISW effect. In fact, the neutrino free-streaming makes the gravitational potential to evolve in time, producing a net $\dot{\Phi} \neq 0$ even in the absence of a recent accelerated background expansion. As shown in [12], neutrino velocities generate an excess of ISW effect at high redshifts z, due to their impact on the linear growth factor. Unfortunately, this effect is not directly observable, since its detection would require very precise data at large l and high redshifts, where the late ISW effect is masked by primordial temperature anisotropies.

The non-linear growth of density perturbations modifies the previous picture, producing additional temperature perturbations which give rise to the so-called "Rees-Sciama" (RS) effect, directly related to the momentum density in the non-linear regime (*e.*g. [13, 14, 15, 16, 17], and references therein). In fact, the accelerated non-linear growth of structure increases the depth of the potential wells in overdense regions, resulting in a reduction of the total CMB temperature, with respect to the linear case. This partially cancels the ISW effect in hotter regions. On the contrary, the RS effect increases the ISW effect in underdense regions, since the saturation of the density contrast in voids further suppresses the growth of the gravitational perturbations. Also in this case, massive neutrinos have an impact, since they alter the RS effect in a scale- and redshift-dependent way, owing to the neutrino free-streaming scale, $\lambda_{\rm fs}$.

Besides the ISW and RS effects, CMB photons undergo also the gravitational lensing [18] and the Sunyaev-Zeldovich (SZ) effects [19] generated by LSS. Massive neutrinos alter the related auto- [20] and cross-correlation functions, with different impacts at the linear and non-linear levels, mainly depending on their effect on the total matter power spectrum and cluster number counts.

In this work, we present for the first time in the literature a full reconstruction of the total (linear and non-linear) ISW-RS effect in the presence of massive neutrinos, together

with its cross-correlations with CMB-lensing and weak-lensing signals. Previous works [21, 22] have provided a similar reconstruction in the standard ΛCDM massless case.

The present analyses make use of all-sky maps extracted via ray-tracing across the "Dark Energy and Massive Neutrino Universe" (DEMNUni) simulations, which are the largest N-body simulations to date with a particle neutrino component. At present, as we explain in more details in § 2 below, these simulations are characterised by a baseline ΛCDM cosmology to which we add neutrinos with different total masses, $M_\nu \equiv \Sigma\, m_\nu$. In the next future, we plan to extend the DEMNUni set with the inclusion of an evolving dark energy background, with different equations of state w, in order to study the degeneracy between M_ν and w at the non linear level.

This paper is organised as follows. In § 2 we present the DEMNUni simulations. In § 3, we explain the map-making procedure, in § 4 we present the ISW-RS and lensing signals extracted from the simulations, focusing the discussion on the angular auto power spectra, and presenting the cross-correlation signals in § 5. Finally, in § 6 we draw our main conclusions.

2. The DEMNUni simulations

The DEMNUni simulations have been conceived for the analysis of different probes, like galaxy surveys and CMB data, and their cross-correlations, in the presence of massive neutrinos. In particular, in order to investigate simultaneously the neutrino impact on different CMB secondary anisotropies, *e.g.* the ISW-RS and weak-lensing effects, we have produced a set of simulations with a volume big enough to include the very large scale perturbation modes, and, at the same time, with a good mass resolution to investigate the effects of small-scale non-linearities and neutrino free-streaming. Moreover, for the accurate reconstruction of the light-cone back to the starting redshift of the simulations, we have assumed an output time-spacing small enough that possible systematic errors, due to the interpolation between neighbouring redshifts along the line of sight, result to be negligible.

The DEMNUni simulations have been performed using the tree particle mesh-smoothed particle hydrodynamics (TreePM-SPH) code GADGET-3 [23], specifically modified by [24] to account for the presence of massive neutrinos. This modified version of GADGET-3 follows the evolution of CDM and neutrino particles, treating them as two separated collisionless species. Given the relatively high velocity dispersion, neutrinos have a characteristic clustering scale larger than the CDM one, allowing to save computational time by neglecting the calculation of the short-range gravitational force. This results in a different spatial resolution for the two components, which for neutrinos is fixed by the PM grid (that we have chosen to be eight times larger than the particle number), while for CDM particles is about one order of magnitude higher.

The DEMNUni set of simulations has a starting redshift $z_{in} = 99$, and is characterised by a comoving volume of $(2\ h^{-1}\ \mathrm{Gpc})^3$ filled with 2048^3 dark matter particles and, where present, 2048^3 neutrino particles. Given the large amount of memory required by the simulations, baryon physics is not included. The authors in Ref. [25] found baryon effects to be independent of cosmological parameters, suggesting that they are also independent of the neutrino mass; therefore, our choice should not affect the results presented in this work. This is supported also by [26], where the authors show that the neutrino induced

suppression in the matter power spectrum is very much the same also when neutrinos are considered in the presence of baryons. Moreover, since we are seeking deviations (due to massive neutrinos) from a fiducial reference ΛCDM model in terms of $P(k)$ ratios, we expect that baryon feedback will cancel out in this case, and that additional effects produced by the interplay of neutrinos with baryon physics should be higher order in both (for further details see [27]).

We have produced a total of four different simulations, choosing the cosmological parameters according to the *Planck* results [28], namely a flat ΛCDM model generalised to a $\nu\Lambda$CDM framework by changing only the value of the sum of the three active neutrino masses $M_\nu = \Sigma\, m_\nu = (0, 0.17, 0.3, 0.53)$ eV, respectively, and keeping fixed $\Omega_{\rm m}$ and the amplitude of primordial curvature perturbations $A_{\rm s}$.

The simulations are characterised by a softening length $\varepsilon = 20\,h^{-1}$ Kpc, and have been run on the Fermi IBM BG/Q supercomputer at CINECA[2], Italy, employing about 1 Million cpu-hrs per simulation (including the production of halo and sub-halo catalogues). For each simulation we have produced 62 output logarithmically equispaced in the scale factor $a = 1/(1+z)$, in the redshift interval $z = 0 - 99$, 49 of which lay between $z = 0$ and $z = 10$. For each of the 62 output times, we have dumped on-the-fly a particle snapshot composed by both CDM and neutrino particles, a three-dimensional (3D) grid of the gravitational potential, Φ, with side size $L_{\rm box} = 2\,h^{-1}$ Gpc and a mesh of 4096^3 cells, and a 3D grid of the time derivative $\dot{\Phi}$, with same dimensions and resolution, for a total of about 90 TB of data per simulation. Finally, in order to build halo catalogues, we have post-processed each of the 62 particle snapshots with the friends-of-friends (FoF) algorithm, included in GADGET-3 [29, 30], setting to 32 the minimum number of particles, thus fixing the halo minimum mass to $M_{\rm FoF} \simeq 2.5 \times 10^{12}\,h^{-1} M_\odot$. Finally, the FoF catalogues have been processed via the SUBFIND algorithm (also included in GADGET-3) so that the initial FoF parent halos are split into multiple sub-halos, with the result of an increase in the total number of identified objects and of a lower minimum mass limit (for further details see [27]).

In Fig. 1 the power spectra extracted from the simulations for two total neutrino masses are shown (upper panel), together with their ratios with respect to the ΛCDM case (lower panel), for different neutrino masses and at two different redshifts. Worth of note is the range of scales sampled by the simulations, more than three order of magnitudes, thanks both to the peculiar large volume and mass resolution characterising the DEMNUni set. The lower panel of Fig. 1 shows the well-known non-linear damping caused by massive neutrinos on the total matter power spectrum. Our findings recover previous results in the literature [31, 32, 33, 34, 35, 36, 37, 38, 39, 40], in particular the excess of power suppression with respect to the linear theoretical expectations. As we will show in the next Sections, the non-linear behaviour of the total matter power spectrum proportionally affects the CMB-lensing and weak-lensing potentials from LSS, and the larger the total neutrino mass M_ν is, the greater its impact on lensing quantities is. On the contrary, we will show that, for the ISW-RS effect, lighter neutrinos produce, at intermediate scales, a larger effect on $\dot{\Phi}$, due to their higher thermal velocities, $v_{\rm th}(z, m_\nu) \simeq 158\,(1+z)\,(1{\rm eV}/m_\nu)\,{\rm km/s}$, and smaller free-streaming comoving wave number in Fourier space, $k_{fs} \equiv 2\pi/\lambda_{fs}/(1+z)$.

[2] http://www.cineca.it/

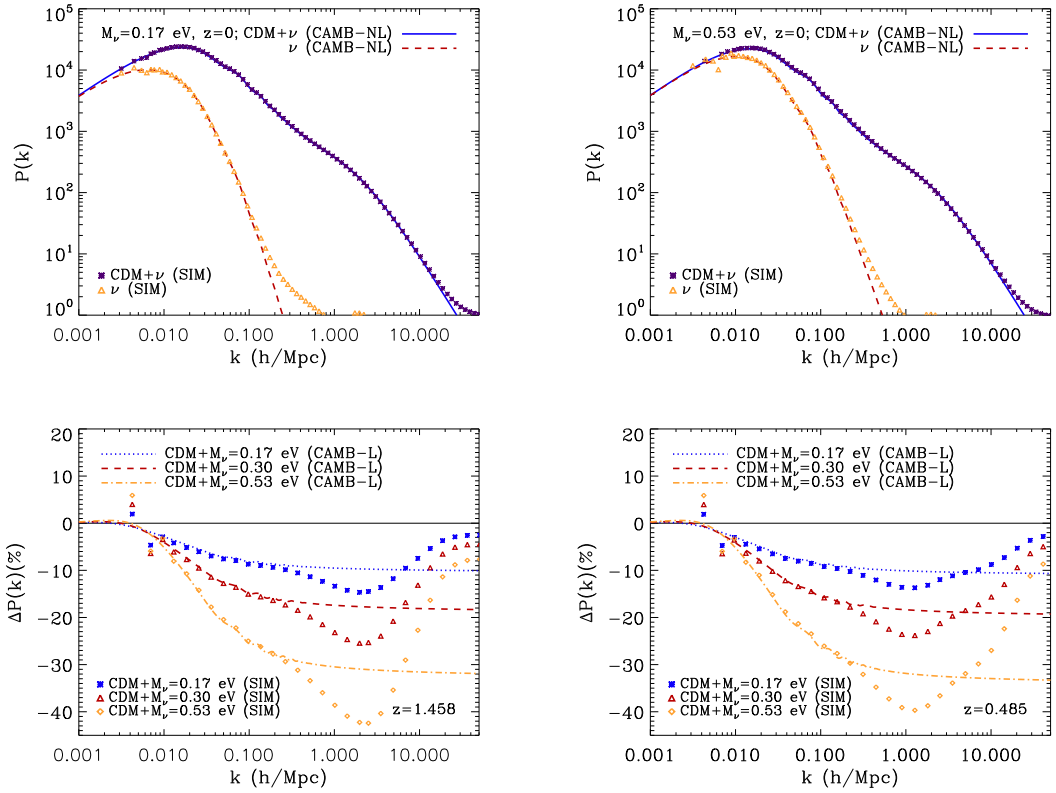

Figure 1: Top panel: the total matter $P(k, z = 0)$ for $M_\nu = 0.17, 0.53$ eV, measured from the simulations (violet stars) compared to the non-linear (NL) total matter $P(k)$ extracted from CAMB (solid blue line) combined with the HALOFIT [41] non-linear corrections, including the neutrino contribution from [26]. Orange triangles and red dashed lines represent the corresponding neutrino $P(k)$ from simulations and CAMB, respectively. Bottom panel: ratios of the simulated total matter $P(k)$ for $M_\nu = 0.17, 0.30, 0.53$ eV (stars, triangles, diamonds, respectively) wrt the simulated $P(k, M_\nu = 0$ eV) at $z = 0.485, 1.458$. The dotted blue, dashed red, and dot-dashed orange lines represent the linear (L) expectations from CAMB.

3. ISW-RS and weak-lensing potential reconstruction

The temperature anisotropies induced by the total (linear and non-linear) ISW-RS effect, in a direction $\hat{\mathbf{n}}$ on the sky, can be computed as the integral of the time derivative of the physical peculiar gravitational potential, $\dot{\Phi}$, along the line of sight from the last scattering (LS) surface to the present epoch at t_0 [6].

$$\Delta T(\hat{\mathbf{n}}) = \frac{2}{c^2}\bar{T}_0 \int_{t_{\rm LS}}^{t_0} \dot{\Phi}(t, \hat{\mathbf{n}})\, dt, \tag{3.1}$$

where t is the cosmic time, $t_{\rm LS}$ the age of the Universe at the LS surface, $\bar{T}_0 = 2.7255$K the today CMB temperature, and c the speed of light. Equation (3.1) can be rewritten as the integral over the radial comoving distance, r,

$$\Delta T(\hat{\mathbf{n}}) = \frac{2}{c^3}\bar{T}_0 \int_0^{r_{\rm LS}} \dot{\Phi}(r\hat{\mathbf{n}})\, a\, dr, \tag{3.2}$$

where $r_{\rm LS}$ is the radial comoving distance to the LS surface, and a is the scale factor of the Universe.

Analogously, the integral for the projected CMB lensing potential due to scalar perturbations with no anisotropic stress reads

$$\phi(\hat{\mathbf{n}}) \equiv -2 \int_0^{r_{\rm LS}} \frac{r_{\rm LS} - r}{r_{\rm LS} r} \, \frac{\Phi(r\hat{\mathbf{n}}; c\eta_0 - r)}{c^2} \, {\rm d}r \,, \tag{3.3}$$

where η_0 is the present conformal time, and Φ is the physical peculiar gravitational potential generated by density perturbations. For the purposes of this work, the line-of-sight integration is made in the so-called "Born-approximation" along the *undeflected* photon path, which, for a given particle mass resolution, results to be accurate at sub-percent level for weak-lensing and CMB-lensing calculations up to $l \lesssim 3000$ [42, 43].

The corresponding deflection-angle integral is

$$\boldsymbol{\alpha}(\hat{\mathbf{n}}) \equiv -2 \int_0^{r_*} \frac{r_{\rm LS} - r}{r_{\rm LS} r} \, \nabla_{\hat{\mathbf{n}}} \frac{\Phi(r\hat{\mathbf{n}}; c\eta_0 - r)}{c^2} \, {\rm d}r \,, \tag{3.4}$$

where $[1/r]\nabla_{\hat{\mathbf{n}}}$ is the two dimensional (2D) transverse derivative with respect to the line-of-sight pointing in the direction $\hat{\mathbf{n}} \equiv (\vartheta, \varphi)$.

We implement Eqs. (3.2)-(3.3) in our code for CMB ray-tracing across the simulated Φ and $\dot{\Phi}$ distributions, in order to produce all-sky ISW-RS and weak-lensing maps, as described in § 3.1 below.

3.1 Map-making procedure

As mentioned in § 2, during the production stage of the DEMNUni simulations, using a properly modified version of GADGET-3, we have dumped on-the-fly 62 cubic grids of Φ and $\dot{\Phi}$, with a mesh of 4096^3 cells, each of $\simeq 0.5 h^{-1}$Mpc on a side[3]. Hence, the field Φ corresponds to the density field of the simulations smoothed on a scale of about $500\,h^{-1}$kpc. This resolution is good enough to resolve scales $\gtrsim 10\ h^{-1}$ Mpc, relevant for the effects analysed in this work. As explained in § 2, the resolution of the N-body simulation (which contains structures down to the gravitational softening length of $20\,h^{-1}$kpc) is much greater, but not necessary for the present study.

In order to build mock all-sky maps of the CMB temperature anisotropies ΔT described in Eq. (3.1), we employ the map-making procedure developed by [44], adapted to the ISW-RS effect, *i.e.* CMB photons are ray-traced along the undeflected line of sight through the 3D field $\dot{\Phi}$. We apply the same kind of ray-tracing also to the 3D Φ-grids, in order to produce the same realisation of the Universe and compute the cross-correlation signal between the ISW-RS temperature maps and the CMB/weak-lensing potential maps.

To this aim, we stack the Φ- and $\dot{\Phi}$-grids around the observer, located at $z = 0$, applying the replication and randomisation procedure designed by [44]. This particular 3D tessellation scheme is required to avoid both the repetition of the same structures along

[3]The gravitational potential itself has been calculated by first assigning the particles to the mesh with the clouds-in-cells mass assignment scheme. The resulting density field has then been Fourier transformed, multiplied with the Green's function of the Poisson equation in Fourier space, and then transformed back to obtain the potential. Also, a slight Gaussian smoothing on a scale r_s equal to 1.25 times the mesh size has been applied in Fourier space in order to eliminate residual anisotropies on the scale of the mesh, and a deconvolution to filter out the clouds-in-cells mass assignment kernel has been applied as well. The time derivative of the gravitational potential has been computed via two-sided differentiation of two potential grids dumped at two different step-times immediately subsequent to the output times of each particle snapshot.

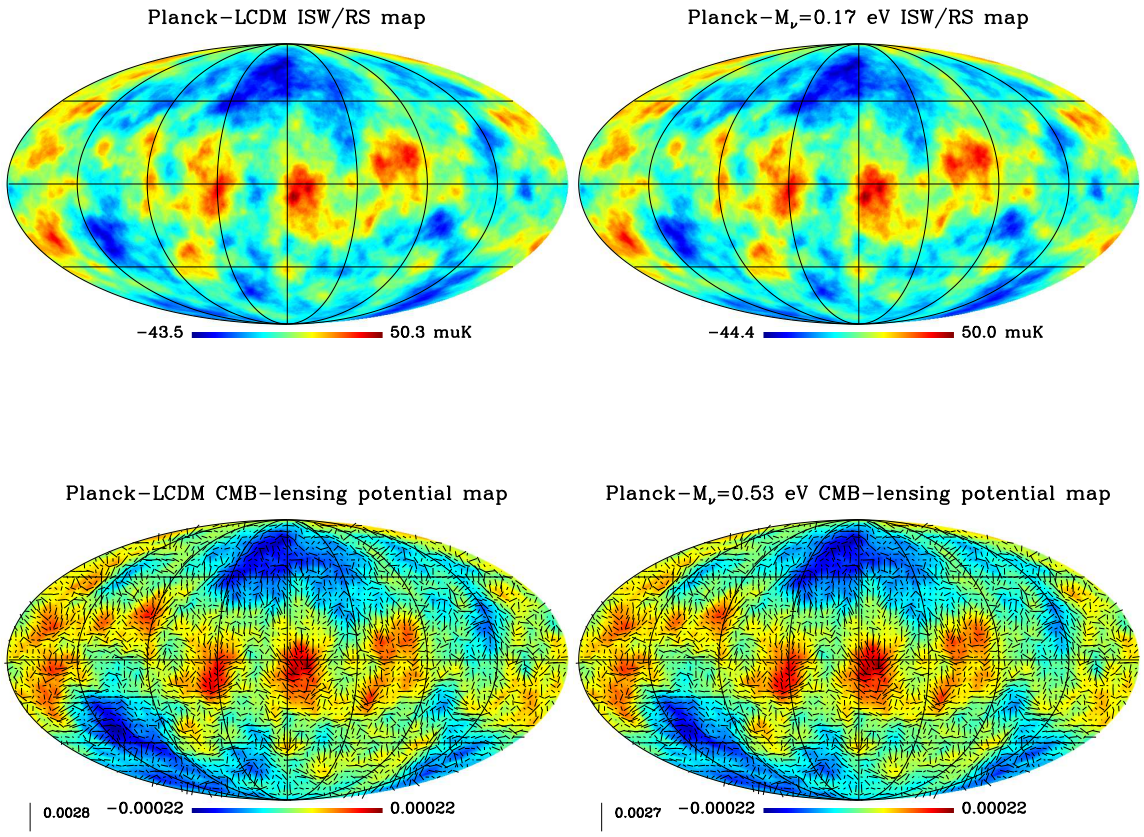

Figure 2: Top panel: projected mono-dipole-subtracted full-sky maps of the ISW-RS signal for $M_\nu = 0$ eV (left) and $M_\nu = 0.17$ eV (right). They do not include primary CMB anisotropies. Bottom panel: projected mono-dipole-subtracted full-sky maps of the lensing potential for $M_\nu = 0$ eV (left) and $M_\nu = 0.53$ eV (right); bars indicate the modulus and orientation of the deflection-angle field $\boldsymbol{\alpha}$.

the line of sight, and the generation of artifacts like ripples in the simulated deflection-angle field, which can be avoided only if the peculiar gravitational potential is continuous transversely to each line of sight. With this procedure we produce a simulated volume around the observer which is large enough to carry out the integration over all the redshifts relevant to this work. Finally, we select a pixelisation of the sky with a set of directions $\hat{\mathbf{n}} \equiv (\vartheta, \varphi)$, following the standard approach introduced by the HEALPix[4] hierarchical tessellation of the unit sphere [45].

In order to extract the impact of massive neutrinos on the ISW-RS effect, mainly dominated by the free-streaming at high redshifts [12], we integrate $\dot{\Phi}$ along the line of sight up to $z \simeq 21$ (for further details on the interpolation and integration scheme see [44]). For the simulated CMB lensing signal, previous studies [46, 47] indicate that an integration up to $z \simeq 99$ is sufficient to recover mostly $\sim 99\%$ of the power. In the case of weak-lensing, we produce all-sky maps of the lensing potential with different source redshifts z_s. In particular, we consider that all the sources are placed on a spherical surface at redshifts

[4]http://healpix.sourceforge.net

$z_s = 2, 5.5, 8$, respectively. This is done for illustrative purposes, *i.e.* to quantify the impact of neutrino free-streaming at different redshifts on the weak-lensing (WL) signal and its cross-correlation with the total ISW-RS effect.

In the upper panel of Fig. 2, we show projected mono-dipole-subtracted full-sky maps of the ISW-RS signal for the massless case (left top panel) and for $M_\nu = 0.17$ eV (right top panel). These maps represent the ISW-RS contribution alone to the CMB temperature, Eq. (3.2), and do not include primary CMB anisotropies. In the lower panel, projected mono-dipole-subtracted full-sky maps of the lensing potential in the two cases, $M_\nu = 0$ eV and $M_\nu = 0.53$ eV, are presented; bars here indicate the modulus and orientation of the deflection angle field which represents the spatial gradient of the lensing potential map, as defined in Eq. (3.4). These maps have been obtained via the map-making technique described above, using a HEALPix pixelisation parameter $N_{\rm side} = 2048$, and have an angular resolution of $\simeq 1.72'$, with 50331648 pixels in total. In Fig. 2, the correlation between the maps in the upper and lower panels, *i.e.* between the ISW-RS and lensing potential realisations, is clearly visible, and shows how the origin of these two effects is due to the same LSS distribution crossed by CMB photons.

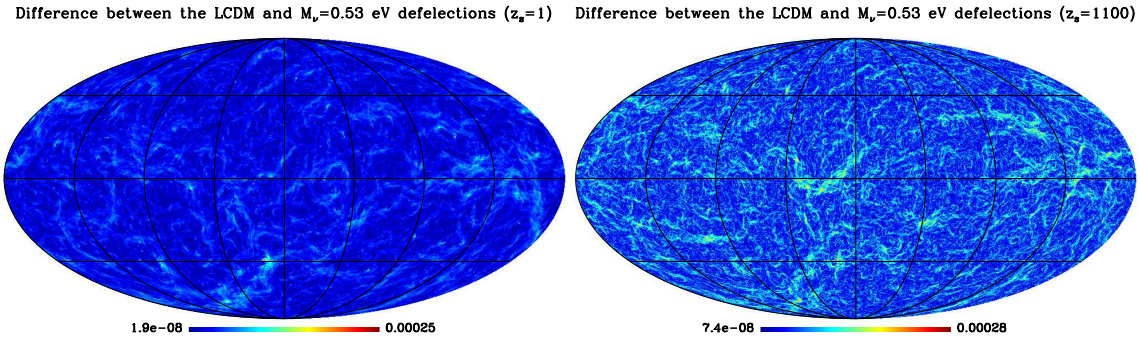

Figure 3: Modulus of the deflection-angle vector difference between the massless case, $M_\nu = 0$ eV, and the massive neutrino case, $M_\nu = 0.53$ eV. Left: all the galaxy sources are supposed to be located at $z_s = 1$. Right: the source is represented by CMB photons at $z_s = 1100$.

4. The impact of massive neutrinos on auto power spectra

Massive neutrinos produce noticeable effects on CMB secondary anisotropies, which in some cases, *e.g.* for large neutrino masses, can be even visually inspected. Let us first notice some visible differences between the massless and massive neutrino cases: in the lower panels of Fig. 2, the neutrino free-streaming suppresses, as expected, the lensing potential signal with respect to the ΛCDM scenario (this can be especially observed by an eye inspection of the filaments in the two maps, and from the bar units of the modulus of the deflection angle); on the other hand, in the upper panels, the effect is opposite, *i.e.* in the ISW-RS case the neutrino free-streaming produces a slight excess of power with respect to the massless case, and this is caused by the $\dot{\Phi}$ induced by hot neutrinos, mostly at high redshifts and for lighter neutrino masses (for this reason the temperature range represented

by the colour bar is larger for the $M_\nu = 0.17$ eV case). We will explain this effect in more details in the next section, but let us anticipate that smaller neutrino masses produce a larger excess in the CMB temperature power spectrum.

In Fig. 3 we show the modulus of the deflection angle difference, between the massless case, $M_\nu = 0$ eV, and the massive neutrino case, $M_\nu = 0.53$ eV. Here the plotted quantity is $\sqrt{(\Delta\alpha_1)^2 + (\Delta\alpha_2)^2}$, where α_1 and α_2 are the two components of the deflection angle $\boldsymbol{\alpha}$, and $\Delta\alpha_i$, with $i = 1, 2$, stands for the difference between each component in the two cases $M_\nu = 0$ eV and $M_\nu = 0.53$ eV. In the left panel all the galaxy sources are supposed to be located at $z_s = 1$, while in the right panel the source is represented by CMB photons at $z_s = 1100$. These maps visually show the suppression in structure formation due to the presence of massive neutrinos, for two different cases of weak-lensing. Given the limited spatial resolution of the potential grids, smaller angular scales are captured via ray-tracing as the source redshift increases, such that the right panel in Fig. 3 shows much more "non-linear" features with respect to the left panel.

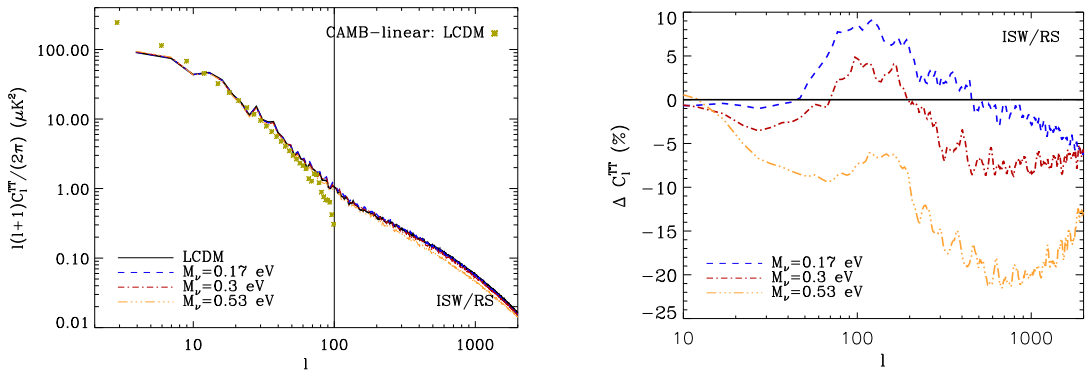

Figure 4: Left: simulated angular power spectra of the total ISW-RS induced temperature anisotropies, for $M_\nu = 0, 0.17, 0.3, 0.53$ eV (black solid, blue dashed, red dot-dashed, and orange tri-dot-dashed lines, respectively). Light-green symbols represent the linear contribution (ISW alone) from CAMB in the massless case, the vertical line at $l \simeq 100$ corresponds roughly to the transition between the linear and non-linear regimes. Right: percent residuals, with respect to the massless case, of the ISW-RS power spectra obtained via direct ray-tracing across the simulations.

4.1 The total ISW-RS effect

The simulated power spectra of the total ISW-RS induced temperature anisotropies, obtained via ray-tracing from $z = 0$ to $z \simeq 21$, are shown in the left panel of Fig. 4 for four different total neutrino masses, $M_\nu = 0, 0.17, 0.3, 0.53$ eV. They are represented by the black (solid), blue (dashed), red (dot-dashed), and orange (tri-dot-dashed) lines, respectively. The light-green symbols represent the linear contribution (ISW alone) from CAMB[5] in the massless case, while the vertical line at $l \simeq 100$ corresponds roughly to the transition between the linear and non-linear regimes [48, 49]. Let us notice the good agreement between the theoretical expectations from CAMB and the simulation outputs at multipoles $l > 10$; at $l < 10$ the simulated signals show a lack of power with respect to the predictions, due to the finite size of the simulation box; on the other hand we

[5] http://camb.info

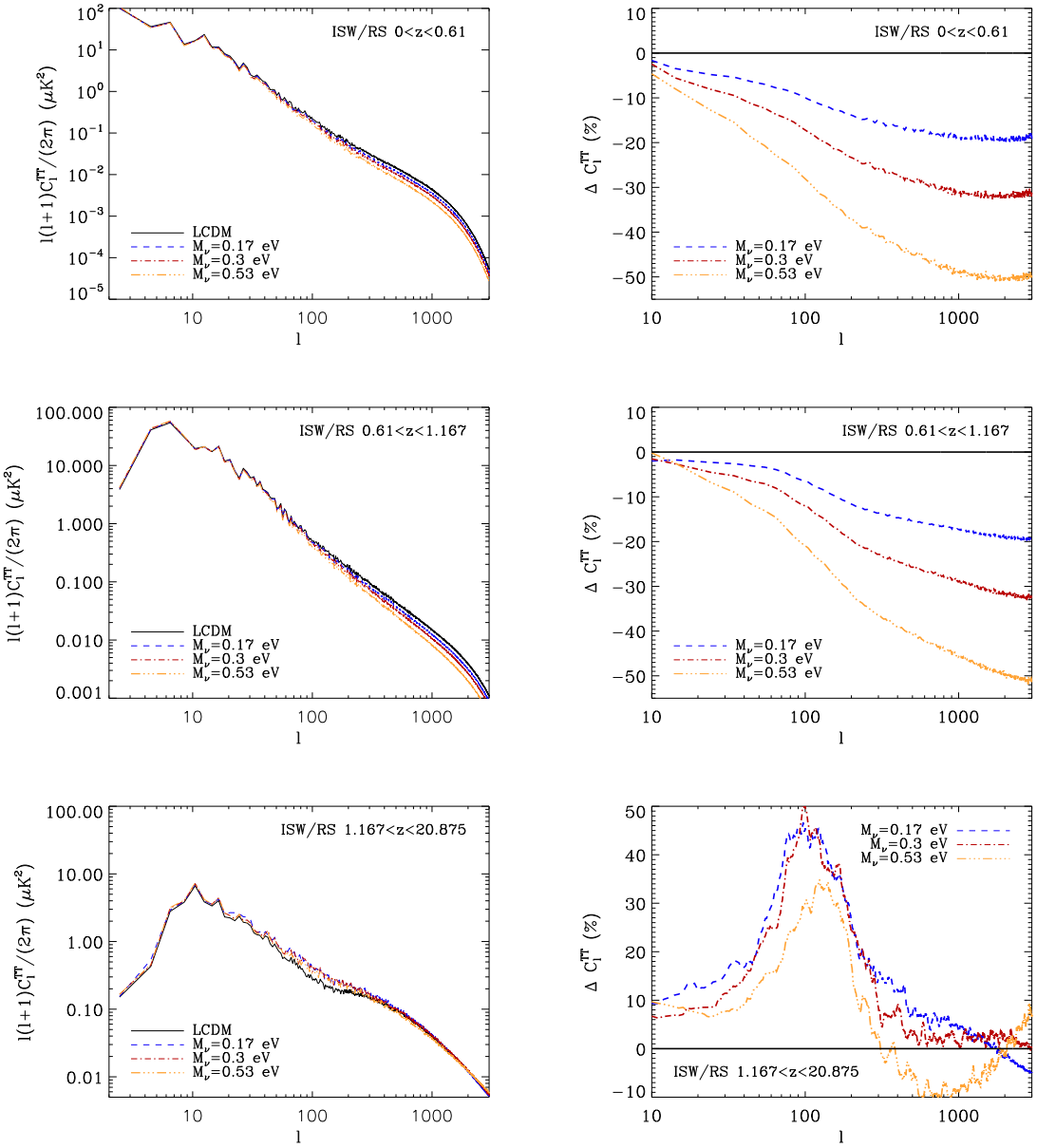

Figure 5: Left: simulated power spectra of the ISW-RS induced anisotropies computed by integration in different redshift bins. Right: corresponding percent residuals with respect to the massless case.

succeed in reproducing the non-linear contribution for $l > 100$, scales at which CAMB predictions fail, given that the RS contribution is not implemented in the code. In the right panel of Fig. 4 it is possible to appreciate the differences produced in the ISW-RS induced temperature anisotropies by free-streaming neutrinos with different total masses. In particular, here we show the percent residuals with respect to the massless case; for small masses, $M_\nu = 0.17, 0.3$ eV, we observe an excess of power of about 10% and 5% respectively, at $50 \lesssim l \lesssim 150$, corresponding to the transition from linear to non-linear regimes. This excess is indeed expected to originate from the $\dot{\Phi}$ term induced by the slow decay of gravitational and matter perturbations produced by hot neutrinos at intermediate

cosmological scales, happening both during the matter and dark energy domination eras. On the other hand, for large neutrino masses, *e.g.* $M_\nu = 0.53$ eV, which correspond to smaller neutrino thermal velocities, the total effect consists in a power suppression, similar to what happens for the lensing potential in the presence of massive neutrinos. Finally, on fully non-linear scales $l > 200$, where the signal is totally due to the RS effect, massive neutrinos decrease the total temperature power with respect to the massless scenario, and this suppression increases with the neutrino mass. This is reasonably due to the non-linear excess of suppression of the total matter power spectra with respect to linear expectations in the presence of massive neutrinos (see the left panel of Fig. 1 for $k \lesssim 10$ h/Mpc, corresponding to the $\dot{\Phi}$-grid resolution), which for lower thermal velocities may dominate the total effect.

In order to understand how the effect of free-streaming massive neutrinos evolves with z, in the left panels of Fig. 5 we show the power spectra of the ISW-RS induced anisotropies computed in different redshift bins. We observe that for low redshifts, $z \lesssim 1$, neutrinos produce a larger suppression in C_l^{TT} at $l > 100$ as their mass increases; in this case the slow down of structure formation in the presence of massive neutrinos has the dominant role. On the other hand, for larger redshifts, $z \gtrsim 1$, far from the epoch of recent acceleration, we see an excess of power which peaks at the transition scale, $l \simeq 100$, and is larger for lighter neutrinos; as pointed out in [12], this is due to the behaviour of the linear growth rate in the presence of massive neutrinos, which produces an evolving gravitational potential even in the absence of dark energy.

More quantitatively, in the right panels of Fig. 5, we show the percent residuals with respect to the ΛCDM case: in the upper panels, for $z \lesssim 1$, the power suppression in the C_l^{TT} has a trend similar to the matter $P(k)$, increasing at large multipoles and somewhat proportional to the neutrino mass ratios. In the lower panel, instead, at higher redshifts, $1 \lesssim z \lesssim 21$, the produced excess of power can even reach 50% for small neutrino masses at $l \simeq 100$. The combination of the lack of power at low redshifts and the excess at high redshifts produces the total effect shown in the left panel of Fig. 4.

Incidentally, let us notice how the impact of the limited simulation volume increases with redshift, producing a larger lack of power at $l < 10$ for larger z values.

4.2 CMB and Weak lensing spectra

Let us now focus the discussion on the effect of massive neutrinos on lens-induced CMB secondary anisotropies. Since lensing traces directly the total matter power spectrum, *i.e.* the gravitational potential Φ rather than the time derivative $\dot{\Phi}$, the theoretical linear predictions from CAMB, combined with the HALOFIT [41] non-linear corrections and including also the neutrino contribution from [26], succeed in reproducing mostly perfectly (as compared to the simulated signal) the CMB-lensing effects in the presence of massive neutrinos on all the scales of interest. This result is presented in the top panels of Fig. 6; in particular, the left panel shows the CMB lensing potential angular power spectrum obtained by photon ray-tracing, from $z = 0$ up to $z = 99$, across the total gravitational field, generated both by CDM and massive neutrinos, from the DEMNUni simulations. The dashed light-green curve represents the prediction from CAMB in the ΛCDM case; the dotted black, blue, red, and orange lines represent the simulated lensing potential for $M_\nu = 0, 0.17, 0.3, 0.53$ eV, respectively. Comparing the black and light-green lines, *i.e.* the ΛCDM curves, we observe less power in the simulated spectrum with respect to CAMB predictions, at multipoles

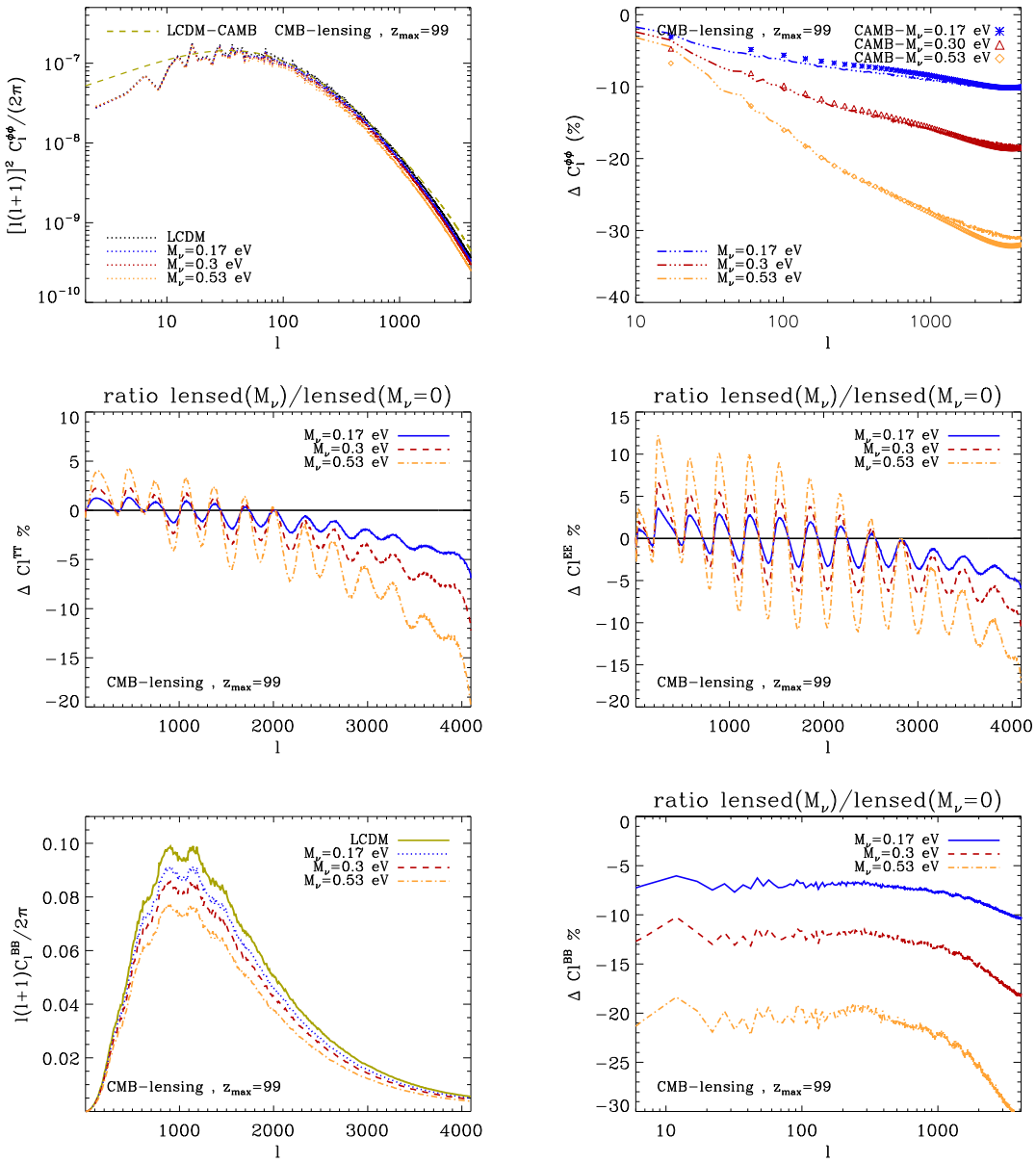

Figure 6: Upper left panel: CMB lensing potential angular power spectrum obtained by photon ray-tracing, from $z = 0$ up to $z = 99$, across the total gravitational field of the DEMNUni simulations. The dashed light-green curve represents the prediction from CAMB in the massless case; the dotted black, blue, red, and orange lines represent the simulated lensing potential for $M_\nu = 0, 0.17, 0.3, 0.53$ eV, respectively. Top right panel: percent residuals between the massive and massless neutrino cases. Here, tri-dot-dashed blue, red, and orange lines are the simulated signals for $M_\nu = 0, 0.17, 0.3, 0.53$ eV, respectively. Semi-analytical non-linear CAMB predictions are represented by symbols, as described in the legend. Middle left panel: percent residuals, wrt to the massless case, of the simulated TT lensed power spectra for $M_\nu = 0.17, 0.3, 0.53$ eV. Middle right panel: percent residuals, wrt to the massless case, of the simulated EE lensed power spectra for $M_\nu = 0.17, 0.3, 0.53$ eV. Lower left panel: simulated lens-induced BB angular power spectra for $M_\nu = 0, 0.17, 0.3, 0.53$ eV. Lower right panel: percent residuals, wrt to the massless case, of the simulated lens-induced BB power spectra for $M_\nu = 0.17, 0.3, 0.53$ eV.

$l \gtrsim 1000$. This is due to the finite resolution of the DEMNUni potential grids, about ~ 0.5 Mpc/h, much smaller compared to the resolution of the dark matter simulations from [50] used for non-linear corrections in HALOFIT. On the other hand, looking at the top right panel of Fig. 6, *i.e.* at the percent residuals between the massive and massless neutrino cases, we do not observe such lack of power with respect to the semi-analytical CAMB predictions (compare tri-dot-dashed lines against symbols), implying that resolution effects cancel out when focusing on the relative differences with respect to the ΛCDM case. In particular, as expected, the integrated effect of massive neutrinos produces a suppression of power in the lensing potential which increases with the neutrino mass, decreases with the angular scale (low l), and at large multipoles tends to become constant, approximately proportional to the ratios of the total neutrino masses. We find an asymptotic power suppression of about $\Delta C_l^{\phi\phi} \simeq 10\%, 19\%, 31\%$ for $M_\nu = 0.17$, 0.30, 0.53 eV, respectively. As mentioned above, this trend is directly related to the behaviour of the total matter power spectra shown in Fig. 1, as the lensing potential power spectrum can be written as the integral along the line of sight of the matter power spectrum weighted by a geometrical factor.

In the middle and lower panels of Fig. 6 we show the effect of massive neutrinos on the lensed CMB temperature (TT), lensed E-mode polarisation (EE), and lens-induced B-mode polarisation (BB) angular power spectra. As in Refs. [46, 43], the lensed power spectra have been obtained by modifying the LENSPIX code[6][51], in order to use directly as input the power spectra and phases of the lensing potential maps produced by ray-tracing across the DEMNUni simulations. As expected, the percent residuals between the massive and massless neutrino cases, presented in the middle panel of Fig. 6, show that free-streaming neutrinos alter the lensed TT and EE power spectra. In particular, as the strength of the gravitational potential decreases for larger neutrino masses, CMB acoustic oscillations are less lensed, *i*.e. they are less smoothed and smeared out than in the massless case. This implies that the larger the neutrino mass is, the larger the lensed TT and EE power spectra are at large angular scales (small l), and the smaller the lensing amplification of the so-called "damping-tail" at small scales (high l) is. As a consequence, the production of the lens-induced B-mode polarisation, via rotation of the E-mode pattern, is less enhanced in the presence of massive neutrinos, and the amplitude of the BB power spectrum decreases with increasing neutrino masses on all the scales, as shown in the left lower panel of Fig. 6. As the right panel shows, the B-mode lack of power due to the presence of massive neutrinos is mostly scale independent (except at $l > 1000$ where non-linear effects come into play) [52, 53]. The reason is well known, *i*.e. B-modes are due to the transfer of E-mode power from small scales to large scales, and on scales $1000 < l < 2000$ the effect of massive neutrinos on E-modes is almost scale-independent, as the right middle panel of Fig. 6 shows. Again, the B-mode power residuals are somewhat proportional, for $l \to 0$, to the ratio of the neutrino masses assumed in the simulations.

Finally, in Fig. 7 we present the results for three cases of weak-lensing, with sources all placed at redshifts $z = 2$, $z = 5.5$, and $z = 8$, respectively. As expected, in all the cases, we find the lensing potential to behave in a way very similar to the CMB lensing potential. In fact, its angular power spectrum is suppressed by free-streaming massive neutrinos, and such suppression is scale dependent, increasing with the multipoles l, as new scales k exceed the free-streaming scale k_{fs}. We have modified CAMB to account for the computation

[6] http://cosmologist.info/lenspix/

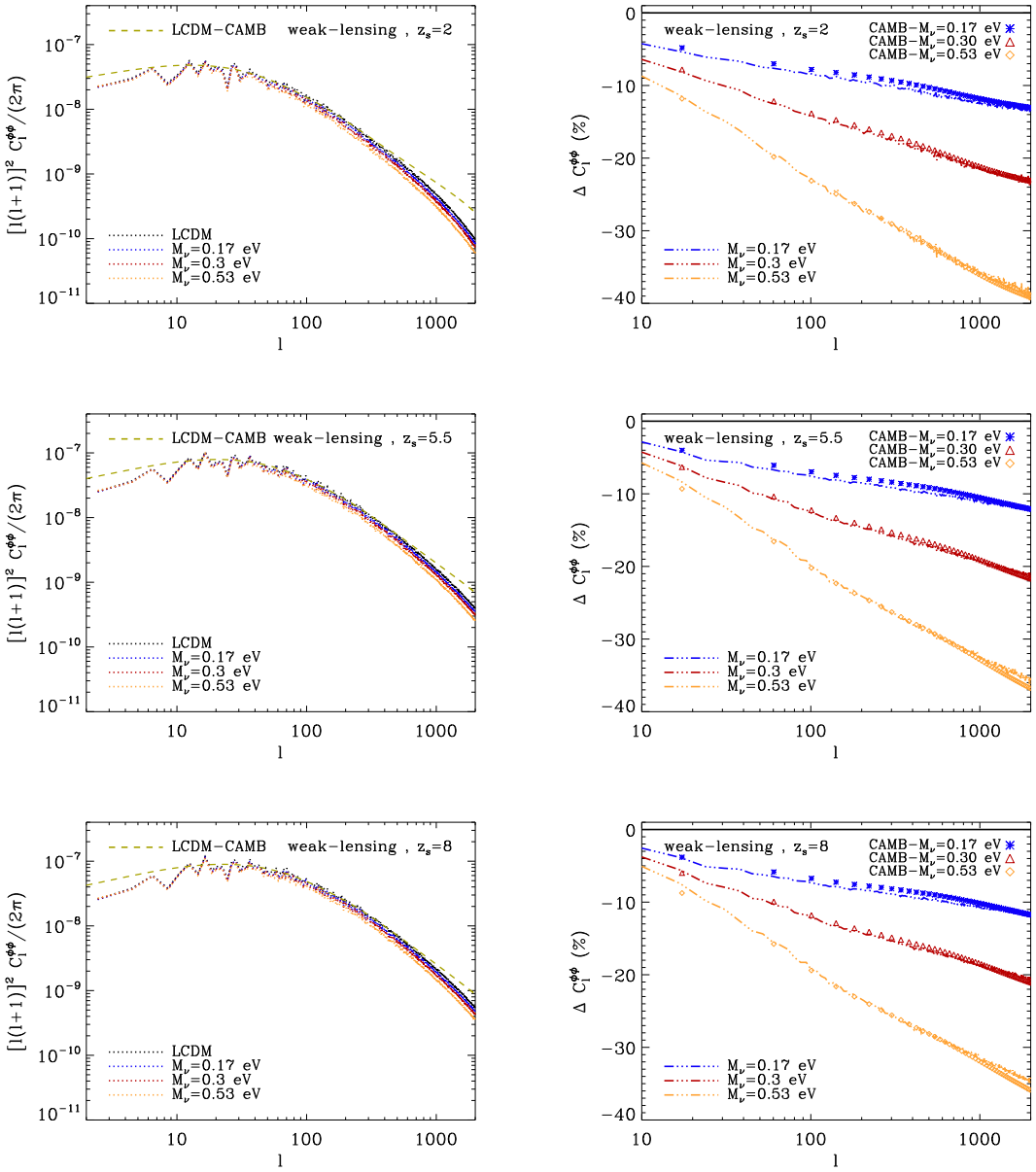

Figure 7: Left: lensing potential angular power spectra for sources all placed at redshifts $z = 2$ (upper panel), $z = 5.5$ (middle panel), and $z = 8$ (lower panel), respectively. The dotted black, blue, red and orange lines represent the simulated signals for $M_\nu = 0, 0.17, 0.3, 0.53\,\mathrm{eV}$, respectively. The ΛCDM non-linear expectations from CAMB are represented by the dashed green line. Right: corresponding percent residuals wrt the massless case. Here, tri-dot-dashed blue, red, and orange lines are the simulated signals for $M_\nu = 0, 0.17, 0.3, 0.53\,\mathrm{eV}$, respectively. Semi-analytical non-linear CAMB predictions are represented by symbols, as described in the legend.

of the weak-lensing signal for sources placed all at the same redshift z_s, by substituting $z_{\rm LS}$ with z_s in the CAMB routine "equations.f90" for the calculation of the "sources(3)" variable; the corresponding analytical expectations are represented by the dashed green line in the left panels of Fig. 7. As expected, given the finite simulation volume, on large scales the simulated signal recovers much better CAMB predictions as redshift decreases,

while on small scales we observe an increase of the lack of power due the limited resolution, ~ 0.5 Mpc$/h$, of the gravitational potential grids used for ray-tracing. Nonetheless, when looking at the relative differences between the massive and massless cases, for different M_ν values, the simulated signal recovers the expectations within the $\sim 1\%$ accuracy level (see the right panel of Fig. 7). This means that the effect of massive neutrinos on LSS formation decouples from highly non-linear regime physics, as *e*.g. baryon effects, since, as well known, massive neutrinos escape the potential field of small scale structures, causing such effects to cancel out when considering relative differences.

5. The impact of massive neutrinos on cross power spectra

Let us now consider the effects of massive neutrinos on the cross angular power spectra between CMB/weak-lensing and the ISW-RS signals. Since the ISW-RS effect is not directly observable, the ISW-RS cross-correlation with weak-lensing (together with its cross-correlation with galaxies, which we do not discuss in this work) allows to observe and measure the impact of time-varying potentials on light travelling to us from the last scattering surface. It is worth noting that here, for the first time in the literature, we present the non-linear behaviour of such cross-correlation signal, as extracted from N-body simulations accounting for free-streaming massive neutrinos. The linear counterpart can be computed using Boltzmann codes as CAMB or CLASS[7] [54].

5.1 ISW-RS–CMB-lensing cross-correlations

The absolute values of the simulated cross power spectra between CMB-lensing and the total ISW-RS induced temperature anisotropies, obtained via ray-tracing from $z = 0$ to $z \simeq 21$, are shown in the left panel of Fig. 8 for four different total neutrino masses, $M_\nu = 0, 0.17, 0.3, 0.53$ eV. They are represented by the black (solid), blue (long-dashed), red (dashed), and orange (dot-dashed) lines, respectively. The violet tri-dot-dashed line represents the linear contribution from CAMB[8] in the massless case. Above all, let us observe that, using a finite box of 2 Gpc$/h$, we manage to recover the predicted linear signal starting from very low multiples, $l \sim 10$. This is a confirmation of the accuracy of the technique implemented to extract the ISW effect from the DEMNUni simulations. In addition, at the transition from linear to non-linear scales, we recover also the expected sign inversion of the cross-correlation spectra due to the negative *non-linear* correlation between the RS effect and matter density, which becomes dominant with respect to the net positive *linear* correlation between density and CMB temperature, produced by the decay of the *linear* gravitational potential, as the Universe expands in the presence of dark energy [55, 56]. This leads to a sign change of the cross-spectrum, which for a ΛCDM model with the same cosmological parameters as in the simulations, happens to be about at $l \sim 700$ [57, 58].

As the left top panel of Fig. 8 shows, the major effect of massive neutrinos on the CMB-lensing/ISW-RS cross spectrum consists of moving the sign inversion position toward larger multipoles, producing a larger displacement as the neutrino mass increases. This can be explained considering that the larger the neutrino mass is, the larger the suppression

[7] http://class-code.net/

[8] As already mentioned in 4.1, at present Boltzmann codes are not able to compute the non-linear contribution to $\dot{\Phi}$.

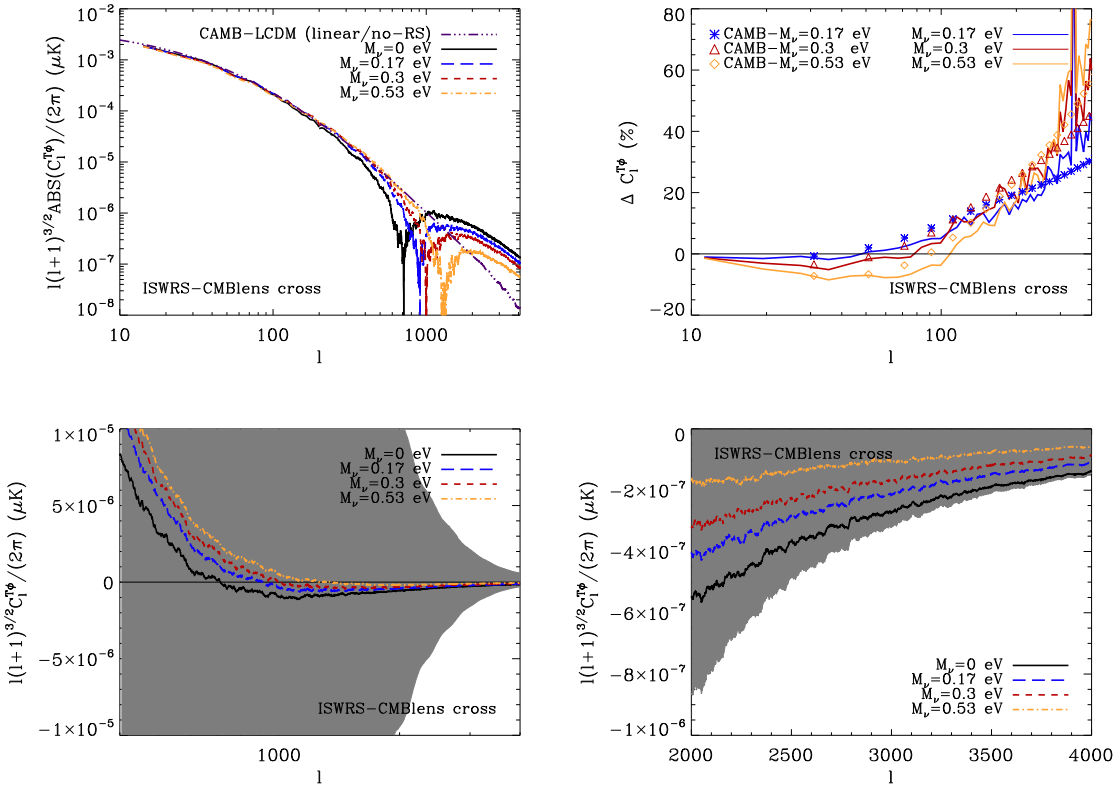

Figure 8: Left upper panel: absolute values of the simulated cross power spectra between CMB-lensing and the total ISW-RS induced temperature anisotropies, obtained via ray-tracing from $z = 0$ to $z \simeq 21$, for $M_\nu = 0, 0.17, 0.3, 0.53$ eV (solid black, long-dashed blue, dashed red, and dot-dashed orange lines, respectively). The violet tri-dot-dashed line represents the linear contribution from CAMB in the massless case. Right upper panel: corresponding percent residuals wrt the massless case on linear scales $l < 400$. Here, blue, red, and orange lines are the simulated signals for $M_\nu = 0, 0.17, 0.3, 0.53$ eV, respectively. Semi-analytical linear CAMB predictions are represented by symbols, as described in the legend. Bottom panels: simulated cross power spectra for $l > 400$. The shaded grey area represents the cosmic variance associated to the signal.

of structure formation is, and therefore cosmological perturbations tend to stay in the linear regime on smaller scales than in the massless case. This implies that free-streaming massive neutrinos not only produce an excess of ISW-RS power, but also an excess of cross-correlation between CMB-lensing and the ISW-RS effect, and this time such excess increases with larger neutrino masses on scales $100 < l < 1000$, being a factor of ~ 4 for $M_\nu = 0.3$ eV, at $l \sim 600$. On multipoles $700 < l < 1000$, the shift of the sign inversion is the the dominant feature, and, indeed, a future detection and measurement of its position could be a further probe of the total neutrino mass. On larger multipoles the asympthotic suppression of the matter power spectra due to neutrino free-streaming becomes dominant, and we recover the usual trend, *i.e.* larger neutrino masses produce a larger decrease of the non-linear cross power spectrum.

In the right top panel of Fig. 8 we compare our findings with CAMB predictions on linear scales. On multipoles $10 < l < 400$ the accuracy of the reconstructed signal is very high, about $1 - 2\%$, and the residuals start to increase only when non-linear effects come

into play, *i.e* at $l > 400$. On such scales, the behaviour of the simulated cross power spectra is shown in the bottom panels of Fig. 8. In particular, the different curves in left panel represent the sign inversion due to non-linearities, and the shaded grey area the associated cosmic variance $\sqrt{[(C_l^{T\kappa})^2 + C_l^{TT} C_l^{\kappa\kappa}]/(2l+1)}$, which unfortunately makes measurements of this effect quite challenging, since the primary CMB temperature anisotropies act as a foreground in this case.

5.2 ISW-RS–weak-lensing cross-correlations

Finally, we consider the cross-correlation between the ISW-RS and the weak-lensing signals. The left panels of Fig. 9 show the cross spectra obtained with lensing sources all placed at $z_s = 2$, 5.5, 8 and for $M_\nu = 0, 0.17, 0.3, 0.53$ eV, represented by the black (solid), blue (long-dashed), red (dashed), and orange (dot-dashed) lines, respectively. The violet tri-dot-dashed line represents the corresponding linear contribution from CAMB, while the light-green dotted line is the linear ISW-RS/CMB-lensing cross spectrum from CAMB, here shown for comparison. As in §5.1, also in this case we find a mostly perfect agreement between CAMB linear predictions and the simulated signals, at scales $30 \lesssim l \lesssim 400$. On smaller multipoles, $l \lesssim 30$ window effects take place producing a lack of power in the simulated cross signal. As for the ISW-RS/CMB-lensing cross spectrum, also in this case on larger multipoles, $l \gtrsim 400$, non-linear effects produce a sign inversion, whose position stays however mostly constant with increasing neutrino masses, even if we notice that it is more shifted toward larger multipoles as z_s increases (as expected from the theory of linear perturbation evolution).

In the right panels of Fig. 9 we show the residuals, with respect to the massless case, of the simulated ISW-RS/weak-lensing cross spectra (solid lines), together with linear predictions from CAMB (symbols). For comparison, we also show corresponding residuals for the simulated weak-lensing auto spectra (tri-dot-dashed lines). For $z_s = 2$ we find an excellent agreement within 1% accuracy; at larger z_s the agreement is still good with an accuracy of about $2 - 3\%$. This lower accuracy is probably due to percent differences in the ISW-RS reconstruction between CAMB and our ray-tracing technique. Overall, at $30 \lesssim l \lesssim 300$ we observe a scale dependent suppression of the cross signal which increases with the neutrino mass. At $l \gtrsim 300$, the trend starts to reverse, and for lighter neutrino masses the cross spectra exceed their value in the massless case.

It is worth to note that the suppression, due to massive neutrinos, of the ISW-RS/weak-lensing cross spectra is smaller than for the weak-lensing auto spectra (compare solid lines against tri-dot-dashed lines). Moreover, while in the latter case this suppression is mostly constant with z_s, in the former case it decreases with the increase of the source redshift, and finally, for very high values of z_s, neutrino free-streaming produces an excess of signal with respect to the massless case, as we observe also in the CMB case to a greater extent. This is due to the larger excess of ISW-RS in the presence of massive neutrinos at higher redshifts, far from dark energy domination at low z (see Fig. 5). This excess somehow balances the suppression in the weak-lensing signal, and was first pointed out by [12] for the case of the ISW-galaxy cross-correlation. Similar arguments explained in their § **B** hold also in our case. It has been also shown [56] that ideal cosmic variance limited experiments may detect, via cross-correlation with lensing, the non-linear RS effect with a significance of $\sim 3\sigma$ integrating up to multipoles $\ell = 3 \times 10^3$. However, this significance is drastically reduced by the finite resolution and noise of actual CMB experiments, so that the signal to

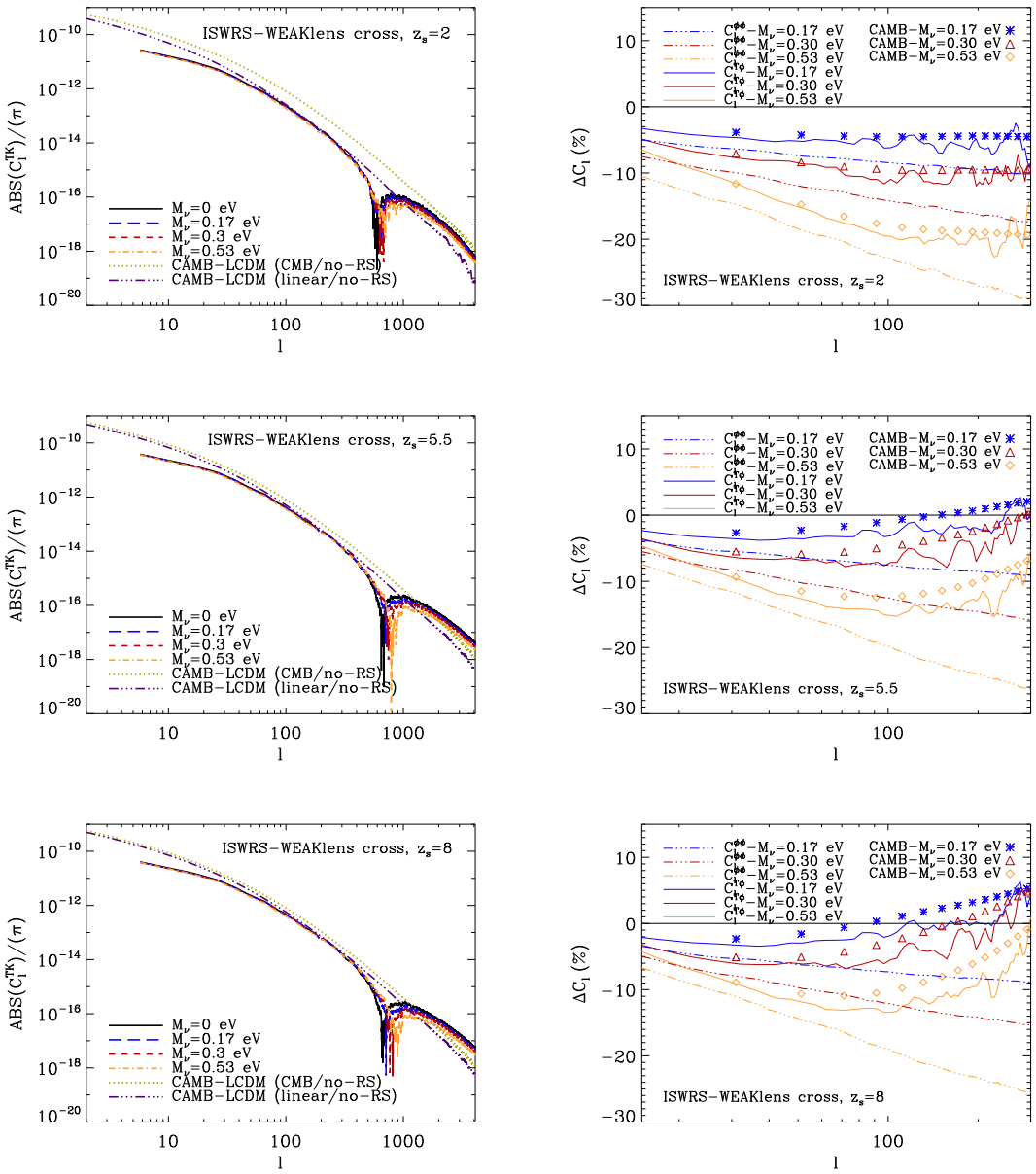

Figure 9: Left: absolute values of the WL/ISW-RS angular cross spectra for sources placed at redshifts $z = 2$ (upper panel), $z = 5.5$ (middle panel), and $z = 8$ (lower panel), respectively. The solid black, long-dashed blue, dashed red, and dot-dashed orange lines represent the simulated signals for $M_\nu = 0, 0.17, 0.3, 0.53$ eV, respectively. The ΛCDM linear expectations from CAMB are represented by the tri-dotted violet line. The light-green dotted line is the linear ISW-RS/CMB-lensing cross spectrum from CAMB, here shown for comparison. Right: percent residuals wrt the massless case for $l < 300$. Tri-dot-dashed blue, red, and orange lines correspond to the simulated signals of the auto WL power spectra for $M_\nu = 0, 0.17, 0.3, 0.53$ eV, respectively. Solid blue, red, and orange lines are the residulars of the simulated ISW-RS/WL cross spectra. The corresponding semi-analytical linear CAMB predictions are represented by symbols, as described in the legend.

noise ratio of the non-linear RS effect results to be an order of magnitude smaller compared to that of the linear ISW effect. This implies that it would be quite difficult to measure it with present and near future CMB-LSS experiments.

Together with the results presented in § 5.1, these represent the main findings of the present work. For the first time in the literature, the cross-correlation between CMB/weak-lensing and ISW-RS effects have been simulated, on a very large range of scales, from the linear to the fully non-linear regimes, and in the presence of massive neutrinos.

6. Conclusions

In this work we present full-sky maps, auto and cross angular spectra of the ISW-Rees-Sciama and CMB/weak-lensing signals, from the linear to the fully non-linear regimes, as extracted via direct ray-tracing across very large N-body simulations including a massive neutrino component, the so-called DEMNUni simulations. We assume a Planck-like baseline cosmology, and add neutrinos with total masses $M_\nu = 0$, 0.17, 0.3, 0.53 eV, fixing the normalisation of the matter power spectrum at CMB.

The analysis of these signals shows that

- Free-streaming massive neutrinos induce a time variation, $\dot{\Phi}$, of the gravitational potential, affecting mostly scales corresponding to the transition from the linear to the non-linear regimes, $l \sim 100$, and producing a non negligible contribution to the ISW effect (see Fig. 4). The induced ΔT anisotropies are more important for light neutrino masses and at high redshifts $z \gtrsim 1.5$, when dark energy is not the dominant component. At lower redshifts the ISW effect becomes more suppressed as the neutrino mass increases (Fig. 5). Considering relative differences with respect to the massless case, on linear scales we recover, within $\sim 1-2\%$, accuracy, analytical expectations from CAMB, which, however, at the moment does not provide non-linear estimations of the ISW-RS signal.

- At non-linear scales, $l > 200$, massive neutrinos decrease the angular power spectrum corresponding to the Rees-Sciama effect. Such suppression is larger for larger neutrino masses, and decreases with increasing redshifts, as shown in Fig. 5.

- Since lensing traces directly the matter power spectrum, which can be largely suppressed for large neutrino masses, we recover a similar suppression in the CMB- and weak-lensing signals (Figs. 6-7). When looking at relative differences with respect to the massless case, the agreement with CAMB (non-linear neutrino corrections included) is at $\sim 1\%$ level on the scales covered by the simulations. The suppression of the lensing auto power spectra decreases with the increase of the source redshift, z_s, with a maximum difference of $\sim 10\%$ between $z_s = 2$ and $z_s = 1100$.

- Lensed TT, EE and BB spectra are consistently affected by massive neutrinos (mid and lower panels of Fig. 6). As expected, since the strength of the gravitational potential decreases for larger neutrino masses, CMB acoustic oscillations are less smoothed and smeared out than in the massless case. This implies that, as the neutrino mass increases, the lensed TT and EE power spectra are larger at small l, and the so-called "damping-tail" is lower at high l. Therefore the amplitude of the lens-induced B-mode power spectrum decreases for larger neutrino masses on all the scales, as shown in the left lower panel of Fig. 6.

- Concerning the cross-correlation between ISW-RS and CMB-lensing signals, at $l \lesssim 400$ we correctly recover the linear signal from CAMB, within $1-2\%$ accuracy (Fig. 8). At the transition between the linear and the non-linear regimes, $l \sim 700$, the simulated signal correctly undergoes the sign-inversion expected by non-linear semi-analytical calculations in the massless case [56, 57, 58]. This feature is interestingly altered by the presence of massive neutrinos, as it moves toward larger multipoles with increasing M_ν, and the displacement, with respect to the $M_\nu = 0$ eV case, can be larger than a factor of 2 for $M_\nu = 0.53$ eV. This is reasonably expected, since massive neutrinos extend the linear regime to smaller scales than in the massless case. Therefore, the cross power between ISW-RS and CMB-lensing increases with larger neutrino masses at $300 \lesssim l \lesssim 1500$, and, *e.*g., at $l \sim 600$, we find an excess of cross power of a factor of ~ 4 for $M_\nu = 0.3$ eV. At higher multipoles, in the fully non-linear regime, we find a suppression of the signal as also occurs for the auto spectra.

- As shown in the left panel of Fig. 9, the cross-correlation between ISW-RS and weak-lensing presents features similar to the ISW-RS cross CMB-lensing signal, with the only difference given by a lower total impact of massive neutrinos. Again, when looking at relative differences with respect to the massless case, at $l \lesssim 300$ we correctly recover, within $1-2\%$ accuracy, the linear signal from CAMB, which does not provide non-linear estimations at the moment. The non-linear sign-inversion of the cross power is still present but less enhanced, while the signal seems to increase with increasing z_s. In particular, the excess of ISW-RS due to the presence of massive neutrinos makes the cross power less suppressed with respect to the weak-lensing auto power, and finally, for very high source redshifts, we observe a net excess of power with respect to the massless case (right panel of Fig. 9).

The last two points represent the main findings of this work. The cross-correlation between the ISW-RS and lensing signals enters the computation of the lensed CMB temperature bispectrum [58]; therefore its correct estimation at the non-linear level from N-body simulations, and the knowledge of the neutrino impact on its amplitude may result to be of extreme importance for the full evaluation of the CMB temperature three-point function [59]. The latter probes the perturbation growth and expansion history of the Universe, and hence can be used to constrain dark energy and neutrino masses [18]. In addition, due to non-linear structure evolution, on very small scales the lensing potential is not a Gaussian field, and consequent additional contributions to the bispectrum may be evaluated directly from the simulated maps obtained via the DEMNUni simulations. We reserve this for future work.

Acknowledgments

C.C. thanks Anna Mangilli, Julien Bel, Emiliano Sefusatti, Matteo Calabrese, and Matteo Zennaro for very useful discussions. C.C. thanks Matteo Viel for providing the N-GenIC code for initial conditions, modified to take into account a massive neutrino particle component. The DEMNUni simulations were carried out at the Tier-0 IBM BG/Q machine, Fermi, of the Centro Interuniversitario del Nord-Est per il Calcolo Elettronico (CINECA,

Bologna, Italy), via the five million cpu-hrs budget provided by the Italian SuperComputing Resource Allocation (ISCRA) to the class–A proposal entitled "The Dark Energy and Massive-Neutrino Universe". C.C. acknowledges financial support from the INAF Fellowships Programme 2010 and from the European Research Council through the Darklight Advanced Research Grant (n. 291521). K.D. and M.P. acknowledge support by the DFG Cluster of Excellence "Origin and Structure of the Universe" and the SFB-Tansregio TR33 "The Dark Universe".

References

[1] J. Lesgourgues and S. Pastor, *Massive neutrinos and cosmology*, *Physics Reports* **429** 307–379, [astro-ph/0603494].

[2] J. Lesgourgues and S. Pastor, *Neutrino mass from Cosmology*, *ArXiv e-prints* [arXiv:1212.6154].

[3] J. Lesgourgues and S. Pastor, *Neutrino cosmology and Planck*, *New Journal of Physics* **16** 065002, [arXiv:1404.1740].

[4] J. Lesgourgues, G. Mangano, G. Miele, and S. Pastor, *Neutrino Cosmology*. Feb., 2013.

[5] G. Rossi, N. Palanque-Delabrouille, A. Borde, M. Viel, C. Yèche, J. S. Bolton, J. Rich, and J.-M. Le Goff, *Suite of hydrodynamical simulations for the Lyman-α forest with massive neutrinos*, *Astronomy & Astrophysics* **567** A79, [arXiv:1401.6464].

[6] R. K. Sachs and A. M. Wolfe, *Perturbations of a Cosmological Model and Angular Variations of the Microwave Background*, *The Astrophysical Journal* **147** 73.

[7] Planck Collaboration, P. A. R. Ade, N. Aghanim, C. Armitage-Caplan, M. Arnaud, M. Ashdown, F. Atrio-Barandela, J. Aumont, C. Baccigalupi, A. J. Banday, and et al., *Planck 2013 results. XIX. The integrated Sachs-Wolfe effect*, *Astronomy & Astrophysics* **571** A19, [arXiv:1303.5079].

[8] Planck Collaboration, P. A. R. Ade, N. Aghanim, M. Arnaud, M. Ashdown, J. Aumont, C. Baccigalupi, A. J. Banday, R. B. Barreiro, N. Bartolo, and et al., *Planck 2015 results. XXI. The integrated Sachs-Wolfe effect*, *ArXiv e-prints* [arXiv:1502.0159].

[9] T. Giannantonio, R. Crittenden, R. Nichol, and A. J. Ross, *The significance of the integrated Sachs-Wolfe effect revisited*, *Monthly Notices of the Royal Astronomical Society* **426** 2581–2599, [arXiv:1209.2125].

[10] A. J. Shajib and E. L. Wright, *Measurement of the integrated Sachs-Wolfe effect using the AllWISE data release*, *ArXiv e-prints* [arXiv:1604.0393].

[11] B. R. Granett, M. C. Neyrinck, and I. Szapudi, *A Map of the Integrated Sachs-Wolfe Signal from Luminous Red Galaxies*, *The Astrophysical Journal* **701** 414–422, [arXiv:0812.1025].

[12] J. Lesgourgues, W. Valkenburg, and E. Gaztañaga, *Constraining neutrino masses with the integrated-Sachs-Wolfe-galaxy correlation function*, *Physical Review D* **77** 063505, [arXiv:0710.5525].

[13] M. J. Rees and D. W. Sciama, *Large-scale Density Inhomogeneities in the Universe*, *Nature* **217** 511–516.

[14] A. Cooray, *Nonlinear integrated Sachs-Wolfe effect*, *Physical Review D* **65** 083518, [astro-ph/0109162].

[15] U. Seljak, *Rees-Sciama Effect in a Cold Dark Matter Universe*, *The Astrophysical Journal* **460** 549, [astro-ph/9506048].

[16] D. N. Spergel and D. M. Goldberg, *Microwave background bispectrum. I. Basic formalism*, *Physical Review D* **59** 103001, [astro-ph/9811252].

[17] P. M. Merkel and B. M. Schäfer, *Contributions to the non-linear integrated Sachs-Wolfe effect: Birkinshaw-Gull effect and gravitational self-energy density*, *Monthly Notices of the Royal Astronomical Society* **431** 2433–2440, [arXiv:1211.3326].

[18] A. Lewis and A. Challinor, *Weak gravitational lensing of the CMB*, *Physics Reports* **429** 1–65, [astro-ph/0601594].

[19] Y. B. Zeldovich and R. A. Sunyaev, *The Interaction of Matter and Radiation in a Hot-Model Universe*, *Astrophysics & Space Science* **4** 301–316.

[20] M. Roncarelli, C. Carbone, and L. Moscardini, *The effect of massive neutrinos on the Sunyaev-Zel'dovich and X-ray observables of galaxy clusters*, *Monthly Notices of the Royal Astronomical Society* **447** 1761–1773, [arXiv:1409.4285].

[21] Y.-C. Cai, S. Cole, A. Jenkins, and C. S. Frenk, *Full-sky map of the ISW and Rees-Sciama effect from Gpc simulations*, *Monthly Notices of the Royal Astronomical Society* **407** 201–224, [arXiv:1003.0974].

[22] W. A. Watson, J. M. Diego, S. Gottlöber, I. T. Iliev, A. Knebe, E. Martínez-González, G. Yepes, R. B. Barreiro, J. González-Nuevo, S. Hotchkiss, A. Marcos-Caballero, S. Nadathur, and P. Vielva, *The Jubilee ISW project - I. Simulated ISW and weak lensing maps and initial power spectra results*, *Monthly Notices of the Royal Astronomical Society* **438** 412–425, [arXiv:1307.1712].

[23] V. Springel, *The cosmological simulation code GADGET-2*, *Monthly Notices of the Royal Astronomical Society* **364** 1105–1134, [astro-ph/0505010].

[24] M. Viel, M. G. Haehnelt, and V. Springel, *The effect of neutrinos on the matter distribution as probed by the intergalactic medium*, *Journal of Cosmology and Astroparticle Physics* **6** 015, [arXiv:1003.2422].

[25] M. P. van Daalen, J. Schaye, C. M. Booth, and C. Dalla Vecchia, *The effects of galaxy formation on the matter power spectrum: a challenge for precision cosmology*, *Monthly Notices of the Royal Astronomical Society* **415** 3649–3665, [arXiv:1104.1174].

[26] S. Bird, M. Viel, and M. G. Haehnelt, *Massive neutrinos and the non-linear matter power spectrum*, *Monthly Notices of the Royal Astronomical Society* **420** 2551–2561, [arXiv:1109.4416].

[27] E. Castorina, C. Carbone, J. Bel, E. Sefusatti, and K. Dolag, *DEMNUni: the clustering of large-scale structures in the presence of massive neutrinos*, *Journal of Cosmology and Astroparticle Physics* **7** 043, [arXiv:1505.0714].

[28] Planck Collaboration, P. A. R. Ade, N. Aghanim, C. Armitage-Caplan, M. Arnaud, M. Ashdown, F. Atrio-Barandela, J. Aumont, C. Baccigalupi, A. J. Banday, and et al., *Planck 2013 results. XVI. Cosmological parameters*, *Astronomy & Astrophysics* **571** A16, [arXiv:1303.5076].

[29] V. Springel, N. Yoshida, and S. D. M. White, *GADGET: a code for collisionless and gasdynamical cosmological simulations*, *New Astronomy* **6** 79–117, [astro-ph/0003162].

[30] K. Dolag, S. Borgani, G. Murante, and V. Springel, *Substructures in hydrodynamical cluster simulations*, *Monthly Notices of the Royal Astronomical Society* **399** 497–514, [arXiv:0808.3401].

[31] F. Villaescusa-Navarro, F. Marulli, M. Viel, E. Branchini, E. Castorina, E. Sefusatti, and S. Saito, *Cosmology with massive neutrinos I: towards a realistic modeling of the relation between matter, haloes and galaxies*, *Journal of Cosmology and Astroparticle Physics* **3** 011, [arXiv:1311.0866].

[32] E. Castorina, E. Sefusatti, R. K. Sheth, F. Villaescusa-Navarro, and M. Viel, *Cosmology with massive neutrinos II: on the universality of the halo mass function and bias*, *Journal of Cosmology and Astroparticle Physics* **2** 049, [arXiv:1311.1212].

[33] J. Brandbyge and S. Hannestad, *Grid based linear neutrino perturbations in cosmological N-body simulations*, *Journal of Cosmology and Astroparticle Physics* **5** 002, [arXiv:0812.3149].

[34] J. Brandbyge, S. Hannestad, T. Haugbølle, and B. Thomsen, *The effect of thermal neutrino motion on the non-linear cosmological matter power spectrum*, *Journal of Cosmology and Astroparticle Physics* **8** 020, [arXiv:0802.3700].

[35] J. Brandbyge and S. Hannestad, *Resolving cosmic neutrino structure: a hybrid neutrino N-body scheme*, *Journal of Cosmology and Astroparticle Physics* **1** 021, [arXiv:0908.1969].

[36] Y. Ali-Haïmoud and S. Bird, *An efficient implementation of massive neutrinos in non-linear structure formation simulations*, *Monthly Notices of the Royal Astronomical Society* **428** 3375–3389, [arXiv:1209.0461].

[37] F. Villaescusa-Navarro, S. Bird, C. Peña-Garay, and M. Viel, *Non-linear evolution of the cosmic neutrino background*, *Journal of Cosmology and Astroparticle Physics* **3** 019, [arXiv:1212.4855].

[38] E. Massara, F. Villaescusa-Navarro, and M. Viel, *The halo model in a massive neutrino cosmology*, *Journal of Cosmology and Astroparticle Physics* **12** 053, [arXiv:1410.6813].

[39] C. Wagner, L. Verde, and R. Jimenez, *Effects of the Neutrino Mass Splitting on the Nonlinear Matter Power Spectrum*, *The Astrophysical Journal Letters* **752** L31, [arXiv:1203.5342].

[40] A. Upadhye, R. Biswas, A. Pope, K. Heitmann, S. Habib, H. Finkel, and N. Frontiere, *Large-scale structure formation with massive neutrinos and dynamical dark energy*, *Physical Review D* **89** 103515, [arXiv:1309.5872].

[41] R. E. Smith, J. A. Peacock, A. Jenkins, S. D. M. White, C. S. Frenk, F. R. Pearce, P. A. Thomas, G. Efstathiou, and H. M. P. Couchman, *Stable clustering, the halo model and non-linear cosmological power spectra*, *Monthly Notices of the Royal Astronomical Society* **341** 1311–1332, [astro-ph/0207664].

[42] S. Hilbert, J. Hartlap, S. D. M. White, and P. Schneider, *Ray-tracing through the Millennium Simulation: Born corrections and lens-lens coupling in cosmic shear and galaxy-galaxy lensing*, *Astronomy & Astrophysics* **499** 31–43, [arXiv:0809.5035].

[43] M. Calabrese, C. Carbone, G. Fabbian, M. Baldi, and C. Baccigalupi, *Multiple lensing of the cosmic microwave background anisotropies*, *Journal of Cosmology and Astroparticle Physics* **3** 049, [arXiv:1409.7680].

[44] C. Carbone, V. Springel, C. Baccigalupi, M. Bartelmann, and S. Matarrese, *Full-sky maps for gravitational lensing of the cosmic microwave background*, *Monthly Notices of the Royal Astronomical Society* **388** 1618–1626, [arXiv:0711.2655].

[45] K. M. Górski, E. Hivon, A. J. Banday, B. D. Wandelt, F. K. Hansen, M. Reinecke, and M. Bartelmann, *HEALPix: A Framework for High-Resolution Discretization and Fast Analysis of Data Distributed on the Sphere*, *The Astrophysical Journal* **622** 759–771, [astro-ph/0409513].

[46] C. Carbone, C. Baccigalupi, M. Bartelmann, S. Matarrese, and V. Springel, *Lensed CMB temperature and polarization maps from the Millennium Simulation*, *Monthly Notices of the Royal Astronomical Society* **396** 668–679, [arXiv:0810.4145].

[47] C. Carbone, M. Baldi, V. Pettorino, and C. Baccigalupi, *Maps of CMB lensing deflection from N-body simulations in Coupled Dark Energy Cosmologies*, *Journal of Cosmology and Astroparticle Physics* **9** 004, [arXiv:1305.0829].

[48] B. M. Schäfer and M. Bartelmann, *Weak lensing in the second post-Newtonian approximation: gravitomagnetic potentials and the integrated Sachs-Wolfe effect*, *Monthly Notices of the Royal Astronomical Society* **369** 425–440, [astro-ph/0502208].

[49] B. M. Schäfer, *Mixed three-point correlation functions of the non-linear integrated Sachs-Wolfe effect and their detectability*, *Monthly Notices of the Royal Astronomical Society* **388** 1394–1402, [arXiv:0803.1095].

[50] R. Takahashi, M. Sato, T. Nishimichi, A. Taruya, and M. Oguri, *Revising the Halofit Model for the Nonlinear Matter Power Spectrum*, *The Astrophysical Journal* **761** 152, [arXiv:1208.2701].

[51] A. Lewis, *Lensed CMB simulation and parameter estimation*, *Physical Review D* **71** 083008, [astro-ph/0502469].

[52] Y. Oyama, A. Shimizu, and K. Kohri, *Determination of neutrino mass hierarchy by 21 cm line and CMB B-mode polarization observations*, *Physics Letters B* **718** 1186–1193, [arXiv:1205.5223].

[53] Y. Oyama, K. Kohri, and M. Hazumi, *Constraints on the neutrino parameters by future cosmological 21 cm line and precise CMB polarization observations*, *Journal of Cosmology and Astroparticle Physics* **2** 008, [arXiv:1510.0380].

[54] D. Blas, J. Lesgourgues, and T. Tram, *The Cosmic Linear Anisotropy Solving System (CLASS). Part II: Approximation schemes*, *Journal of Cosmology and Astroparticle Physics* **7** 034, [arXiv:1104.2933].

[55] R. E. Smith, C. Hernández-Monteagudo, and U. Seljak, *Impact of scale dependent bias and nonlinear structure growth on the integrated Sachs-Wolfe effect: Angular power spectra*, *Physical Review D* **80** 063528, [arXiv:0905.2408].

[56] B. M. Schäfer, A. F. Kalovidouris, and L. Heisenberg, *Parameter estimation biases due to contributions from the Rees-Sciama effect to the integrated Sachs-Wolfe spectrum*, *Monthly Notices of the Royal Astronomical Society* **416** 1302–1310, [arXiv:1010.1096].

[57] A. Mangilli, B. Wandelt, F. Elsner, and M. Liguori, *Optimal bispectrum estimator and simulations of the CMB lensing-integrated Sachs Wolfe non-Gaussian signal*, *Astronomy & Astrophysics* **555** A82, [arXiv:1303.1722].

[58] A. Lewis, *The full squeezed CMB bispectrum from inflation*, *Journal of Cosmology and Astroparticle Physics* **6** 023, [arXiv:1204.5018].

[59] A. Lewis, A. Challinor, and D. Hanson, *The shape of the CMB lensing bispectrum*, *Journal of Cosmology and Astroparticle Physics* **3** 018, [arXiv:1101.2234].